UCLA
UCLA Previously Published Works

Title
Effects of Gentle Topography on Forest-Atmosphere Gas Exchanges and Implications for Eddy-Covariance Measurements

Permalink
https://escholarship.org/uc/item/2c61820k

Journal
Journal of Geophysical Research: Atmospheres, 125(11)

ISSN
2169-897X

Authors
Chen, Bicheng
Chamecki, Marcelo
Katul, Gabriel G

Publication Date
2020-06-16

DOI
10.1029/2020jd032581

Copyright Information
This work is made available under the terms of a Creative Commons Attribution-NoDerivatives License, available at https://creativecommons.org/licenses/by-nd/4.0/

Peer reviewed

eScholarship.org Powered by the California Digital Library
University of California

Effects of Gentle Topography on Forest-Atmosphere Gas Exchanges and Implications for Eddy-Covariance Measurements

Bicheng Chen[1], Marcelo Chamecki[1], Gabriel G. Katul[2,3],

[1]Department of Atmospheric and Oceanic Sciences, University of California, Los Angeles, California, USA
[2]Nicholas School of the Environment, Duke University, Durham, NC, USA
[3]Department of Civil and Environmental Engineering, Duke University, Durham, NC, USA

Key Points:

- Topography-induced flow structure causes strong heterogeneity in fluxes of gases emitted in forests
- Flux heterogeneity is not reduced with increasing measurement height
- Implications for tower-based eddy-covariance measurements are discussed

Corresponding author: Marcelo Chamecki, `chamecki@ucla.edu`

Abstract

The interpretation of tower-based eddy-covariance (EC) turbulent flux measurements above forests hinges on three key assumptions: (1) steadiness in the flow statistics, (2) planar homogeneity of scalar sources or sinks, and (3) planar homogeneity in the flow statistics. Large eddy simulations (LES) were used to control the first two so as to explore the break-down of the third for idealized and real gentle topography such as those encountered in Amazonia. The LES runs were conducted using uniformly distributed sources inside homogeneous forests covering complex terrain to link the spatial patterns of scalar turbulent fluxes to topographic features. Results showed strong modulation of the fluxes by flow features induced by topography, including large area with negative fluxes compensating "chimney" regions with fluxes almost an order of magnitude larger than the landscape flux. Significant spatial heterogeneity persisted up to at least two canopy heights, where most eddy-covariance measurements are performed above tall forests. A heterogeneity index was introduced to characterize and contrast different scenarios and a topography categorization was shown to have predictive capabilities in identifying regions of negative and enhanced fluxes.

1 Introduction

Plant canopies such as forests and crops are major sources or sinks of gases including water vapor, carbon dioxide, ozone, and a variety of biogenic volatile organic compounds. The strength of these sources and sinks as well as their temporal dynamics is now routinely quantified using turbulent flux measurements near the canopy-atmosphere interface. The deployment of eddy-covariance (EC) systems on towers has become the standard method to measure scalar fluxes and now serves as ground truth for model evaluation. The majority of some 500 sites contributing data to FLUXNET network (Baldocchi et al., 2001; Baldocchi, 2008) use single point EC measurements to characterize scalar fluxes from a large region of relatively uniform surface cover. The validity of this approach hinges on the representativeness of the point where the tower is located. Typically, single-point EC-based turbulent flux measurements above canopies can be interpreted as landscape fluxes under stationary conditions, in the absence of subsidence or other mean advective terms, and for planar homogeneous source or sink strength distribution within the canopy (Baldocchi et al., 2000). However, such niceties remain rare in practice and the application of EC observations can lead to biased estimations of landscape fluxes even for gentle topographic variations (Katul et al., 2006; Belcher et al., 2012).

The focus of this work is on the canopy-atmosphere gas exchanges from a horizontally uniform forest situated on gentle topography for a neutrally stratified stationary atmospheric flow. Under these conditions, all the spatial variability of scalar fluxes is caused by topography-induced flow features, not variability in scalar sources or sinks or heterogeneity in canopy aerodynamic or physiological properties. Flow inside canopies covering cosine hilly terrain are known to experience flow separation leading to a recirculation region on the lee side of topographic features (Finnigan & Belcher, 2004; Poggi & Katul, 2007; Belcher et al., 2012). Early wind tunnel investigations of flow over forested and non-forested hills showed that forests reduced the velocity at the crest of the hill and led to an earlier flow separation (Ruck & Adams, 1991). Analytical solutions for the mean momentum balance within a uniform dense plant canopy covering a gentle (i.e., with small slopes) isolated hill were also used to explore the onset of recirculation (Finnigan & Belcher, 2004). Further extension of the theory led to the conclusion that the critical slope for flow separation over a canopy-covered hill is much lower than that over a hill covered with short roughness (Ross & Vosper, 2005), the latter being accurately predicted by (Wood, 1995). This effect was mainly explained by a balance between the adverse pressure gradient on the lee-side of the hill and the distributed canopy drag force (absent in rough surfaces). This dominant balance is caused by complete momentum absorption in the deep canopy layer, where turbulent fluxes (and their gradients) are small. Other work extended these arguments by including longitudinal advection and mean vertical velocity-pressure interactions, but the generic features of the recirculation zone were not altered (Poggi et al., 2008). Most of these features have been supported by LES studies of idealized topography such as isolated ridges (Dupont et al., 2008) and hills (Patton & Katul, 2009; Liu et al., 2019). The few studies that include real topography have focused on steeper slopes, for which separation would occur even in the absence of canopy cover (e.g., Grant et al., 2015, 2016; Liu et al., 2016).

The effects of flow separation on the transport of scalars emitted within the canopy has been recently explored using elementary topography (such as isolated hills or sinusoidal ridges, where one mode of topographic variability is considered) in flume experiments and numerical simulations. The flow separation and the recirculation region lead to strong spatial variability of scalar fluxes with enhanced fluxes in the separation region (Katul et al., 2006; Ross, 2011). This effect is stronger for gases emitted near the ground than for gases emitted near the canopy top (Ross & Harman, 2015; Chen et al., 2019). Flume experiments (Poggi & Katul, 2007) and numerical simulations (Chen et al., 2019) revealed that the transport of fluid parcels out of the canopy in the flow separation region is mostly carried by turbulent eddies (and not by the mean recirculating flow), displaying periodic cycles of gas accumulation within the canopy and ejection out of the canopy. The separation point is a region of horizontal flow convergence, and the build up of concentration inside the canopy at this location is promoted by horizontal advection (Chen et al., 2019) towards the recirculation zone. The increased transport out of the canopy at the separation point reflects a large effective footprint inside the canopy, and this phenomenon was termed the "chimney effect" (Chen et al., 2019). No systematic study has been performed over real topography to assess the role or persistence of such chimney effect on turbulent fluxes above the canopy.

To progress on this issue, scalar fluxes over gentle forested topography were determined using large eddy simulations (LES) and then analyzed by extending an earlier study (Chen et al., 2019) in two ways: (1) unlike the prior study that focused on escape of air parcels released inside the canopy, gas fluxes were quantified by tracking particles moving into and out of the forest, and (2) results from an idealized topography consisting of sinusoidal ridges were also contrasted with those obtained from a small region of real topography from the Amazon forest.

2 Methods

2.1 Numerical modeling

Large eddy simulation (LES) was employed to generate the three-dimensional flow field within and above the forest canopy, and a Lagrangian tracking model to study gas transport. In the LES, a distributed drag force modeled by the quadratic drag law was used to represent the main effects of the solid canopy on the flow (Shaw & Schumann, 1992; Pan et al., 2014). An immersed boundary method (IBM) with a signed-distance function was employed to represent the topography on a cartesian grid (Peskin, 1972; Chester et al., 2007), and a second-order accurate smoothing method (Li et al., 2016) to reduce the Gibbs phenomenon at the fluid-solid interface caused by the pseudo-spectral discretization. Lagrangian trajectories were determined using the resolved velocities from the LES and a subgrid-scale velocity obtained from a Langevin equation (Weil et al., 2004). Particle positions were integrated using the stable scheme described by Bailey (2016). A more complete description of the model is given elsewhere (Chen et al., 2019).

2.2 Simulation setup

We employed three simulations to assess the effects of topography on the flux of gases emitted from forests: (i) over flat topography, (ii) over an idealized topography with sinusoidal ridges, and (iii) over real topography. All simulations were designed to represent the Amazon forest near the K34 research tower (Tóta et al., 2012; Fuentes et al., 2016). A summary of simulation parameters is listed in Table 1. The flat topography and the sinusoidal topography are the cases S0.0 and S0.2 described in Chen et al. (2019).

Variables	Symbols	Idealized	Real	Flat
Horizontal domain size (m)	$L_x \times L_y$	2000×1000	3000×3000	2000×1000
Vertical domain size (m)	L_z	540	540	515
Horizontal grid resolution (m)	$dx \times dy$	6.25×6.25	8×8	6.25×6.25
Vertical grid resolution (m)	dz	2	2	2
Mean topography height (m)	$\langle z_t \rangle$	25.00	26.46	0
Canopy height (m)	h_c	39	39	39
Leaf area index (m^2/m^2)	LAI	7.0	7.0	7.0
Pressure gradient acceleration (m/s^2)	$\frac{1}{\rho}\frac{\mathrm{d}p_0}{\mathrm{d}x}$	3.11×10^{-4}	3.11×10^{-4}	3.11×10^{-4}
Total number of Lagrangian parcels	N	1.71×10^{8}	3.42×10^{8}	3.42×10^{7}
Time step (s)	dt	0.1	0.1	0.1

Table 1. Configuration used in numerical simulations.

The forest canopy was assumed to be horizontally homogeneous and continuous across the entire domain. The leaf area density (LAD) profile $a(z)$ was based on data from Tóta et al. (2012) reported in Fuentes et al. (2016), with a total leaf area index $LAI = 7$ m^2/m^2 and a canopy height $h_c = 39$ m (note that estimates of LAI in the region near the K34 tower vary between 6.1 (Marques Filho et al., 2005) and 7.3 (Tóta et al., 2012), and prior simulation for this region have used LAI of 6.0 (Gerken et al., 2017) or 7.0 (Chen et al., 2019)). The resulting canopy adjustment length (Belcher et al., 2003) was $L_c = 1/(C_d \overline{a}) = 13.9$ m, where $\overline{a} = 0.18$ m^{-1} was the average LAD of the canopy and C_d was the drag coefficient assumed constant. Note that for the idealized and real topographies we have $L_c/\Delta x \approx 2.2$ and $L_c/\Delta x \approx 1.7$, respectively (even though these ratios would be concerning in the simulation of forest edges, for the homogeneous canopy used here this was not deemed a problem).

In the idealized topography case, the topography height $z_t(x)$ was described by a cosine function (Figure 1a). The idealized topography shape was defined by a ridge height $H = 50$ m (twice of the amplitude of the cosine function) and a ridge half-length $L = 250$ m (one forth of the topography wavelength), where the nomenclature follows Finnigan and Belcher (2004). The canopy was categorized as a deep canopy because $h_c/L_c > 1$ (Finnigan & Belcher, 2004; Poggi et al., 2008).

For the real topography simulation we selected a region centered at $-2.413°$ S, $-60.504°$ W, because it was characterized by gentle topography and no large-scale valleys or ridges. This ensured that the flow could be properly represented in a relatively small domain (3km $\times$ 3 km). The topography was obtained from the NASA shuttle radar topography mission (SRTM) global 1 arc second data (Werner, 2001; Farr et al., 2007), which has a horizontal resolution of about 30 meters. A simple bilinear scheme was applied to interpolate the topography data to the grid resolution of the simulation. Then, to conform with periodic boundary conditions required by the pseudo-spectral discretization in the LES, a special smoothing was applied to the topography on the edges of the domain. Details about the edge smoothing process and the original topography are provided in the Text S1 in the supporting information, while the final topography used in the simulation is presented in Figure 2a.

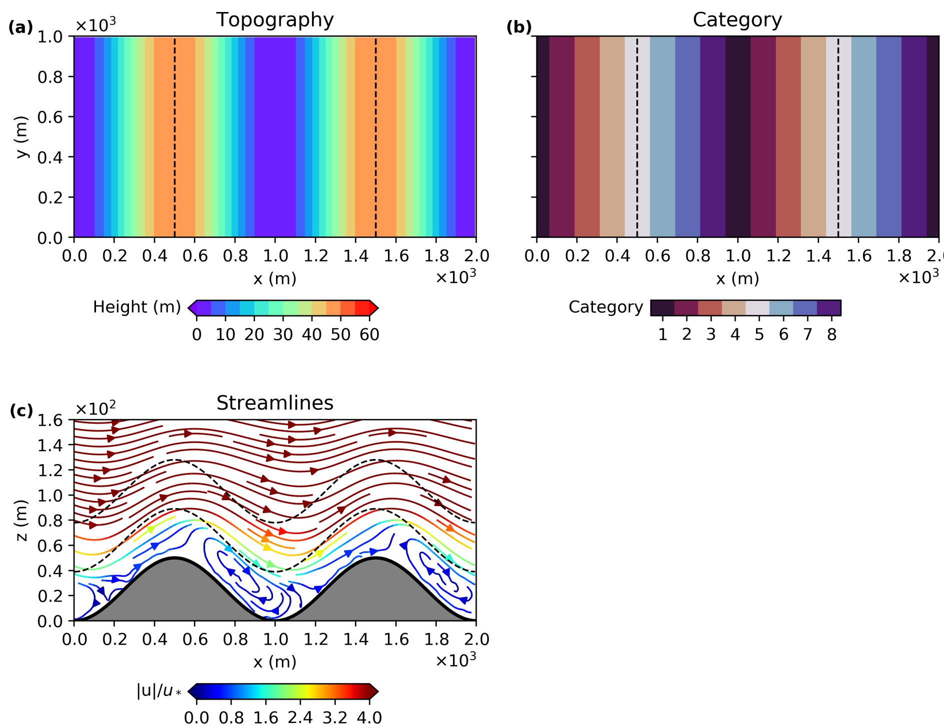

Figure 1. (a) Topography, (b) topography categorization, and (c) mean flow streamlines on the xz-plane for the ideal topography simulation. The black dashed lines in (a) and (b) indicate the location of ridge crests. The black dashed lines in (c) indicate $Z_m/h_c = 1$ and $Z_m/h_c = 2$. Notice that the aspect ratio is not one in panel (c).

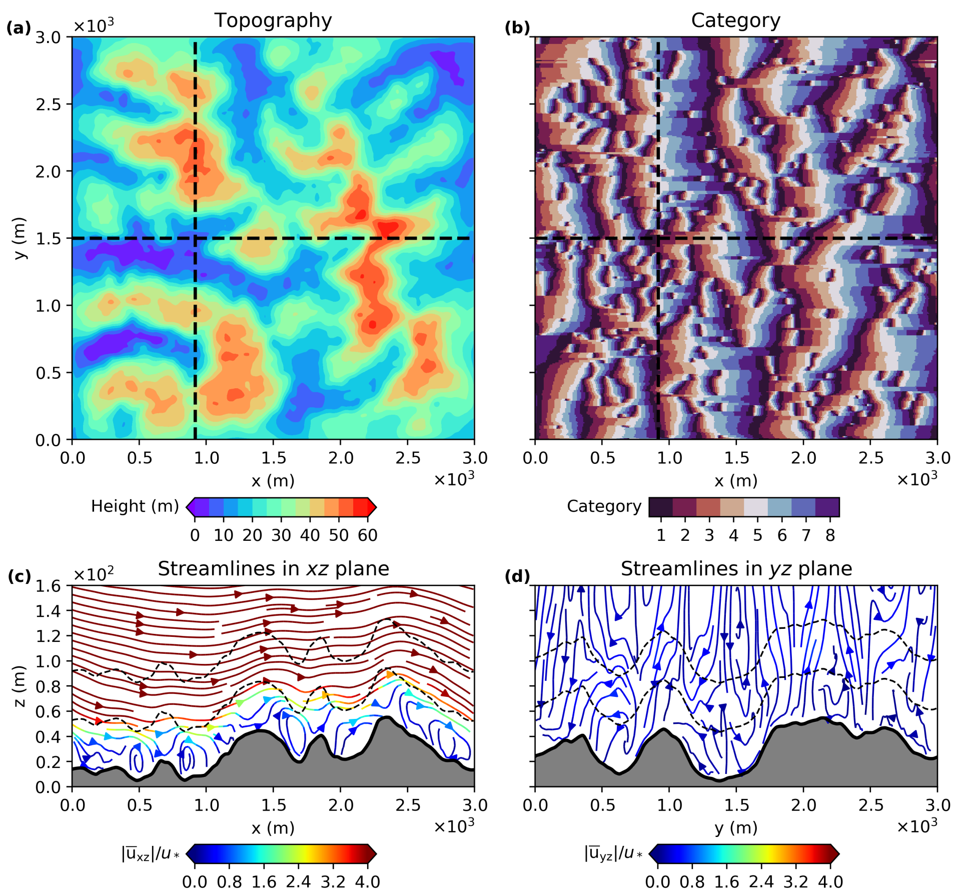

Figure 2. (a) Topography, (b) topography categorization, and mean flow streamlines on the (c) xz-plane and (d) yz-plane for the real topography simulation. The black dashed lines in (a) and (b) indicate the location of the cross-sections shown in (c) and (d), respectively. The black dashed lines in (c) and (d) indicate $Z_m/h_c = 1$ and $Z_m/h_c = 2$. Notice that the aspect ratio is not one in panels (c) and (d).

All simulations were driven by a constant mean pressure gradient force (corresponding to an acceleration of 3.11×10^{-4} m/s^2) in the streamwise direction with no thermal stratification and no buoyancy fluxes. For the simulation without topography, this resulted in a friction velocity of approximately 0.4 m/s. Coriolis effects were neglected due to the low latitude of the selected region. A wall model was applied at the ground surface and a free-slip condition with a damping layer was applied at the top of the domain. A logarithmic mean velocity profile perturbed with random noise was used as initial condition. Simulations were integrated for 8 hours in total, and three-dimensional velocity fields from the last 5 hours were saved every second to run the Lagrangian tracking model.

In the Lagrangian tracking model, air parcels were released from 19 levels equally spaced between 1 m and 37 m above the ground. For data analysis purposes, these 19 source levels were further categorized into 4 layers: the lowest source height, characterizing near-ground emissions and termed "near-surface source"; the remaining 18 source heights were equally divided into three layers characterizing emissions in the "lower", "middle" and "upper" canopy. The initial horizontal positions of air parcels were randomly assigned from a uniform distribution, and a large number of air parcels (see Table 1) were released to guarantee statistical convergence. Air parcel releases were evenly distributed during the 5-hour simulation, and the last 4 hours corresponding to statistical steady state for particle concentration and fluxes were used. Parcel trajectories were integrated with 0.1 s time interval and the motion of each particle trajectory was terminated once its horizontal displacement reached one domain length or width to prevent double counting in the flux and footprint function. The position and velocity of each parcel were recorded each time it crossed one of three sampling heights $Z/h_c = 1$, 1.5, and 2, where $Z = (z - z_t)$ is the height above ground. These records were used to calculate the total flux across the three sampling heights $\overline{F}(x, y)$ and the source area contributing to that flux. These fluxes correspond to the total time averaged values (including the mean flux and the turbulent flux) in the direction perpendicular to the topography (and to the canopy top). Only for the flat case and in special locations for the topography cases, this flux corresponds to the vertical flux. The horizontal grid resolution of the flux calculation was 33 m $\times$ 33 m. We interpreted the local time averaged flux $\overline{F}(x, y)$ as representative of a tower measurement (using a planar-fit coordinate system) and the horizontally averaged flux $\langle\overline{F}\rangle$ as representative of the landscape flux. Thus, only when $\overline{F}(x, y)/\langle\overline{F}\rangle \approx 1$, the local measurements can be considered as representative of the landscape fluxes.

3 Results

3.1 Characteristics of the mean flow

For the idealized topography, mean flow separation was observed right after the top of the ridge, and the recirculation flow spanned the entire vertical extent of the canopy (Figure 1c). This result has been previously reported (Chen et al., 2019) and explained by conventional arguments (Finnigan & Belcher, 2004): the canopy was deep compared to the adjustment length ($h_c/L_c = 2.8 > 1$) so that the momentum transported from the air layer above the canopy was mostly absorbed by the upper canopy, not being able to penetrate the entire canopy layer. The turbulent momentum flux gradient in the vertical was small near the ground, so that the dominant balance was between the topography-induced crest-oriented pressure gradient force and the drag force. This balance produced an inverse flow on the leeward side of the ridge, leading to flow separation.

In the real topography case, flow can go around topographic features such as hills, producing a complex pattern. However, the main pattern in the streamwise direction was similar to the idealized topography, with flow separation and recirculation regions downstream of every major topographic feature (Figure 2c). Even fairly small hills such as the small bump at $x = 250$ m in Figure 2c generated flow separation with a recirculation region. The spanwise direction was dominated by secondary flow structures, which tended to be weaker than the streamwise recirculation regions. These secondary flow structures were not as clearly connected to the spanwise topography as the streamwise patterns, being driven in large part by streamwise flow structures and conservation of mass.

3.2 Gas fluxes above the canopy

For the simulation over flat topography, the scalar fluxes at all three measurement heights were approximately independent of horizontal location and equal to the landscape flux as expected, except for small randomly distributed deviations caused by statistical sampling (not shown). Results for the idealized topography were in stark contrast with those for flat topography, displaying organized regions of enhanced fluxes and regions with negative fluxes (Figure 3). The region of enhanced fluxes was located downwind from the crest, near the separation point, consistently with the chimney effect (Chen et al., 2019) and with other previous model results (Katul et al., 2006; Ross, 2011; Ross & Harman, 2015). The amplitude of the enhanced fluxes depended on the combination of source height and sampling height, with the largest fluxes being almost one order of magnitude larger than the landscape fluxes in the worst case scenario of near-surface emissions with sampling at canopy top (Figure 1a). The negative flux region downwind of the trough in the topography was caused by the persistent mean flow directed into the canopy in this region (see Figure 1c), which carried gas exported through the chimney back into the forest. The negative fluxes were also large, with magnitude comparable to the landscape flux. This dynamics led to a pattern of positive and negative fluxes that was "attached" to the topography. Sampling fluxes at twice the canopy height led to a modest reduction in the flux enhancement, but it increased the magnitude of the negative fluxes (Figure 3b). As the gas source was moved from the near-surface layer to the upper canopy, a progressive reduction in the amplitude of the pattern was observed, reaching a minimum for sources positioned at the canopy top (Figure 3c). This was, in part, because sampling was very close to the source and there was less time for the flow organization to modulate transport. Note that, contrary to intuition, elevating the sampling height amplified the non-uniformity of the fluxes for sources near the canopy top (Figure 3d). This result may seem contradictory to those from Ross and Harman (2015), who showed a decrease in non-uniformity with increasing height. However, the apparent contradiction is caused by the different choice in coordinate systems: Ross and Harman (2015) uses a global cartesian coordinate system, and while their vertical flux becomes more uniform with height, the opposite is observed for the horizontal flux. Results presented here consider fluxes across surfaces parallel to the topography, which combine vertical and horizontal fluxes.

Results were similar for the real topography case (Figure 4), where the flux patterns were clearly connected to the topographical organization in the streamwise direction. The chimney effect still produced regions of large flux enhancement at every separation point (i.e., on the leeward side of each hill). The negative fluxes had larger magnitude than those in the idealized topography and even for the sources in the upper canopy with sampling at canopy top, negative fluxes were larger in magnitude than the landscape flux (Figure 4c). The similarity of the fluxes sampled at $Z_m/h_c = 2$ for sources near the surface and in the upper canopy was remarkable (Figures 4b,d), suggesting that the flux patterns observed at this height were mostly determined by the flow field above the canopy.

As a means to further quantify the flux non-uniformity, we defined the cumulative normalized flux as the maximum fraction of the total normalized flux contributed by a fraction of the total area. This was obtained by integrating the flux sorted in a monotonically decreasing fashion. Mathematically, we represented this via $CF(A_f)$, where A_f is the area fraction increasing monotonically from 0 to 1, and CF is the cumulative flux integrated over the area fraction. For a uniform flux, such as that from flat topography,

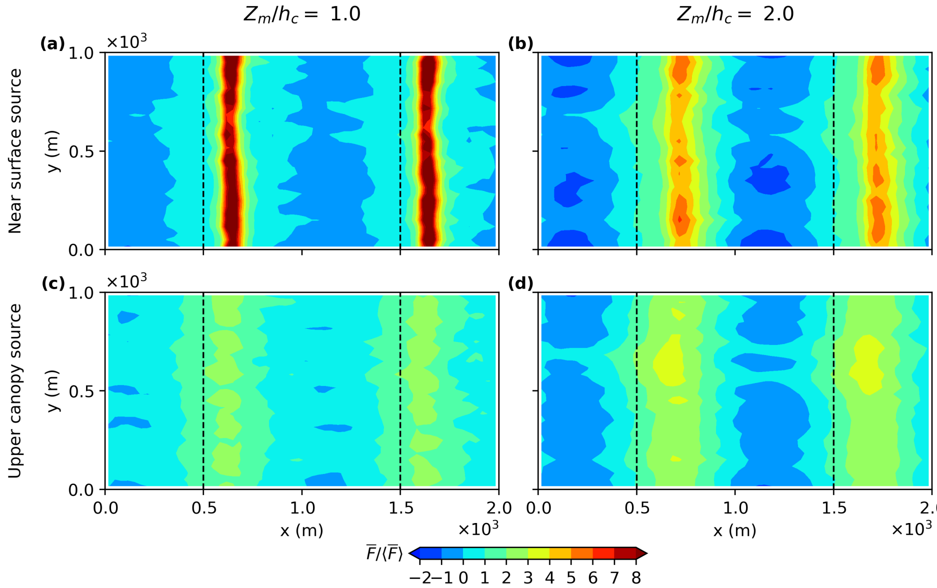

Figure 3. Normalized fluxes $\overline{F}(x,y)/\langle\overline{F}\rangle$ from the ideal topography simulation for different combinations of source layers and sampling heights. Mean wind is from left to right. The black dashed lines indicate the location of ridge crests.

$CF(A_f) = A_f$. For nonuniform flux distributions, $CF(A_f)$ first increases faster than the uniform case and then slower, due to the sorting of the fluxes in the integration. The resulting curves for $CF(A_f)$ are shown in Figure 5, where the curve for a uniform flux is also shown for comparison. Note that the cumulative fluxes are not monotonic due to the presence of negative fluxes. The black dashed line indicates 50% of the total flux over the entire domain and its intercept with any CF gives the minimum fraction of the total area contributing to 50% of the flux. As an example, take the most uniform case of upper canopy source with sampling at canopy top for the idealized topography (red dashed line in Figure 5a). The CF shows that approximately 50% of the flux originates from the 25% of the total area, and 80% of the flux from 50% of the area. There are almost no regions with negative fluxes, as the circle marking the peak in the CF is almost at 100% of the area. In contrast, for the near surface source (blue dashed line), 50% of the fluxes originates from only 5% of the area and almost 35% of the area corresponds to negative fluxes, as the maximum in the CF is close to 65% of the area. Note that for almost all the combinations of source height and sampling height, and for both idealized and real topography, less than 20% of the area contributes 50% of the total flux.

When interpreting the cumulative scalar fluxes, two key variables must be considered: the slope of the curves at the low area fractions (a measure of the intensity of the chimney effect) and the maximum value of the CF, which is a measure of the strength of negative fluxes. A few general trends in the flux heterogeneity can be identified in the results presented in Figure 5. The real topography showed less sensitivity to source height than the idealized case, and the sensitivity decreased with increasing sampling height for both cases. The real topography case showed a more pronounced influence of negative fluxes, not necessarily in terms of spatial extension, but rather in total integrated value.

As one bulk measure of flux non-uniformity, a heterogeneity index G_h can be introduced, which is defined as the area between the cumulative flux CF for any given case

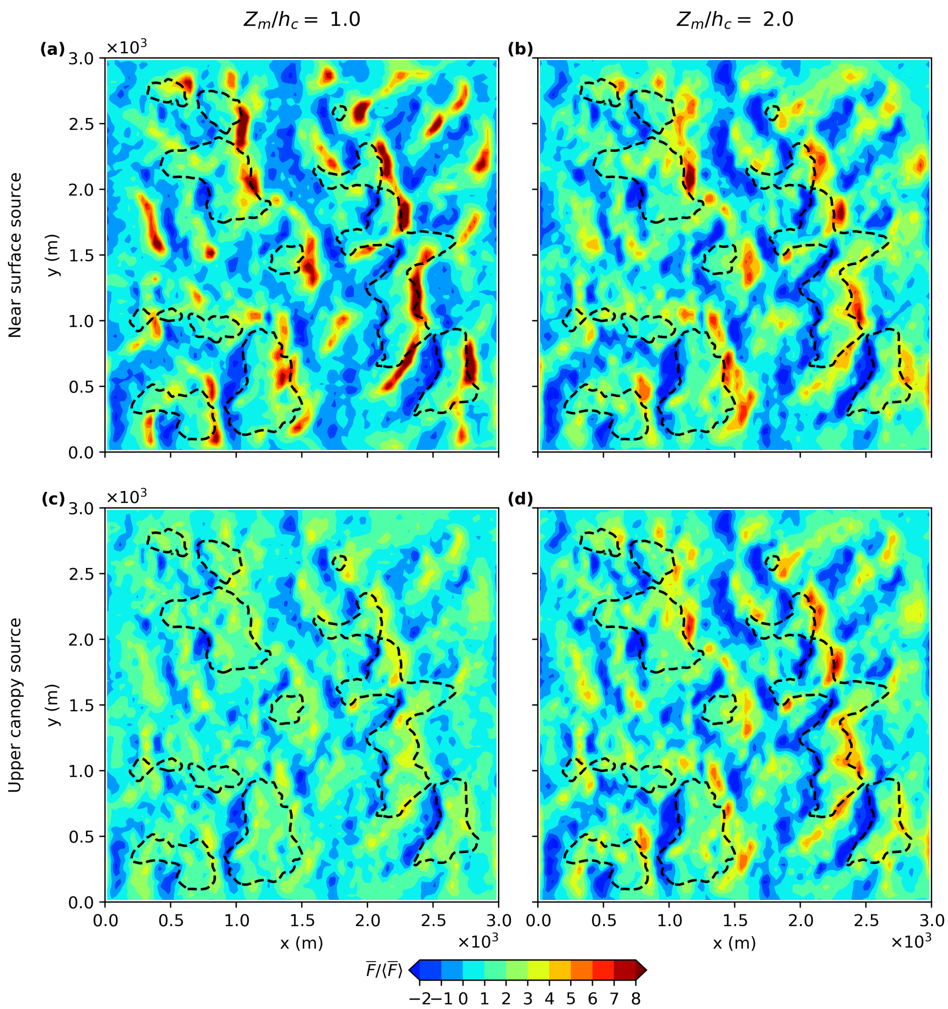

Figure 4. Normalized fluxes $\overline{F}(x, y)/\langle\overline{F}\rangle$ from the real topography simulation for different combinations of source layers and sampling heights. Mean wind is from left to right. The black dashed lines indicate the location where $z_t = 40$ m.

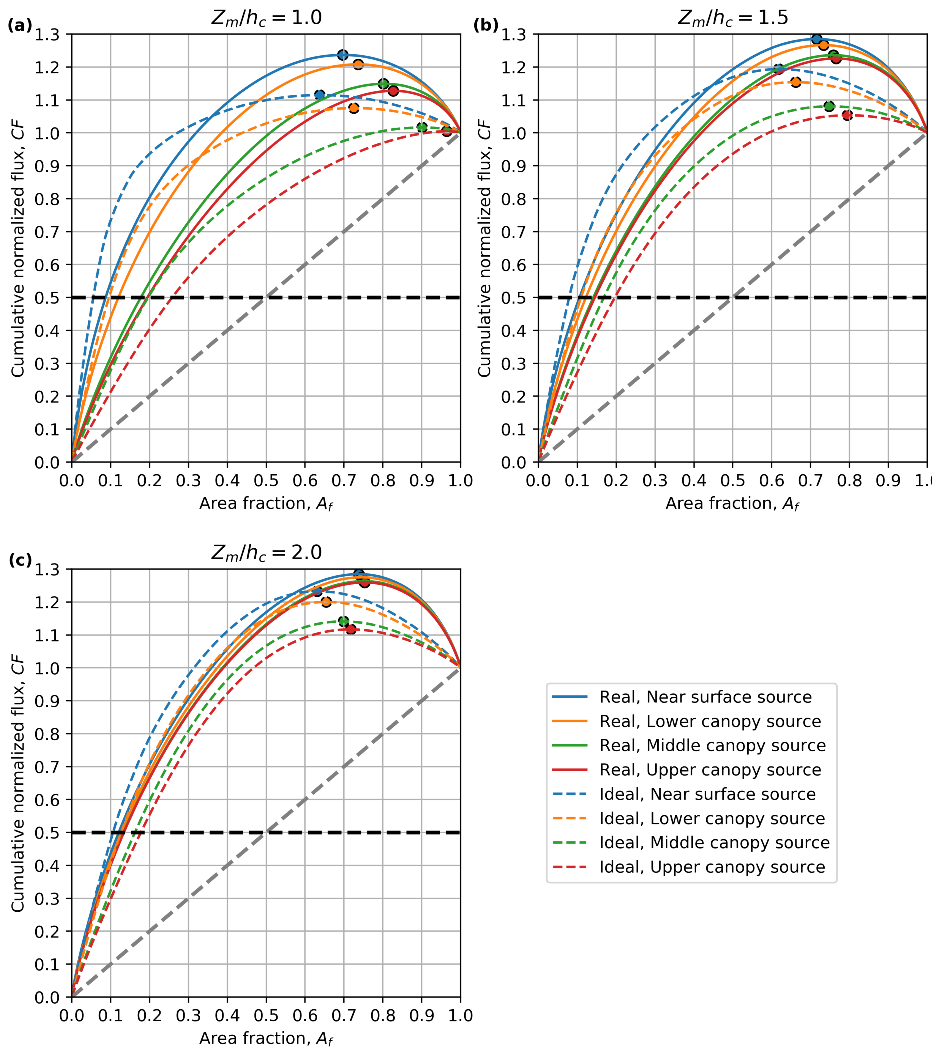

Figure 5. Cumulative normalized fluxes as a function of area fractions at different sampling heights: (a) $Z_m/h_c = 1.0$, (b) $Z_m/h_c = 1.5$, and (c) $Z_m/h_c = 2.0$. The gray dashed line indicates behavior for a uniform flux and the black dashed line indicate 50% of the total flux. The dot on each curve marks the maximum cumulative distribution function.

and the uniform case (labeled CF_u), normalized by the uniform case. That is,

$$G_h = \frac{\int_0^1 [CF(A_f) - CF_u(A_f)]\mathrm{d}A_f}{\int_0^1 CF_u(A_f)\mathrm{d}A_f} = 2\int_0^1 CF(A_f)\mathrm{d}A_f - 1. \quad (1)$$

The index G_h is analogous to the Gini index used in economics to quantify wealth distribution from a Lorenz curve representation (Lorenz, 1905). Similarly to the Gini index, the minimum value $G_h = 0$ represents uniform fluxes and as the flux become less uniform the value of G_h increases. However, differently from the Gini that is bounded by 1, G_h does not have an upper bound because fluxes can be negative. Values of G_h are given in Table 2 and some interesting, more quantitative characterizations can be made. For all combinations of source and sampling heights, fluxes over the real topography were less uniform than over the ideal topography. In addition, lower sources always produced less uniform fluxes than sources higher up in the canopy even though the differences became less pronounced as sampling height increased. Finally, increasing sampling height had small influence on the non-uniformity of fluxes from the near surface and lower canopy, increasing significantly the non-uniformity of fluxes from the middle and upper canopy.

Source layer	**Sampling height**	**Heterogeneity index**		**Mean source area**		
		Ideal	**Real**	**Flat**	**Ideal**	**Real**
Near surface	1	0.97	1.00	2.27	4.16	5.40
	1.5	0.99	1.01	4.44	8.11	8.88
	2	0.97	0.97	7.86	11.12	12.30
Lower canopy	1	0.80	0.89	0.92	2.42	5.31
	1.5	0.87	0.95	2.72	7.29	10.15
	2	0.89	0.94	6.01	12.08	15.34
Middle canopy	1	0.51	0.70	0.30	0.65	1.83
	1.5	0.67	0.87	1.65	2.96	6.63
	2	0.75	0.92	4.79	7.62	12.65
Upper canopy	1	0.38	0.64	0.20	0.39	1.12
	1.5	0.58	0.85	1.74	2.42	5.82
	2	0.70	0.91	4.92	6.50	11.94

Table 2. Heterogeneity index (G_h) and mean source area contributing 50% of the total flux (Ω_{50} in $\times 10^4$ m^2).

3.3 Categorization of topography

It is evident from Figures 3 and 4 that the flux patterns share strong resemblance with the topography underneath (albeit with some phase-differences due to advection). To further explore this fact, we designed a topography categorization based on the results for the idealized case. We first divided the topography wavelength into 8 equal segments labeled category 1-8, with the category 1 centered on the trough and category 5 centered on the crest (Figure 1b). Because the flux patterns were strongly related to the streamwise topography, in the real topography case only the streamwise direction was taken into account. The categorization proceeded by finding two consecutive crests in the streamwise direction, and splitting the crest–trough distance into 5 categories (1 to 5) and the trough–crest distance into another 5 (5 to 8 and then 1). This procedure resulted in a complex pattern (Figure 2b). In the real topography, the area assigned to a crest is asymmetric because the upwind and downwind troughs are not equally spaced from the crest (the same is true for the area around troughs).

We calculated average fluxes conditioned on topography category, $\langle \overline{F}/\langle \overline{F} \rangle | cat \rangle$, and the corresponding standard deviations. Results for the idealized topography (Figure 6) presented large differences between categories with little variability within each category, pointing to a strong coupling between topography and flux. The only exception to this was the peak flux for near-ground and deep-canopy sources, for which the signature of the chimney is concentrated in a narrow region causing large variability within the category where the chimney is (Figure 6a,b).

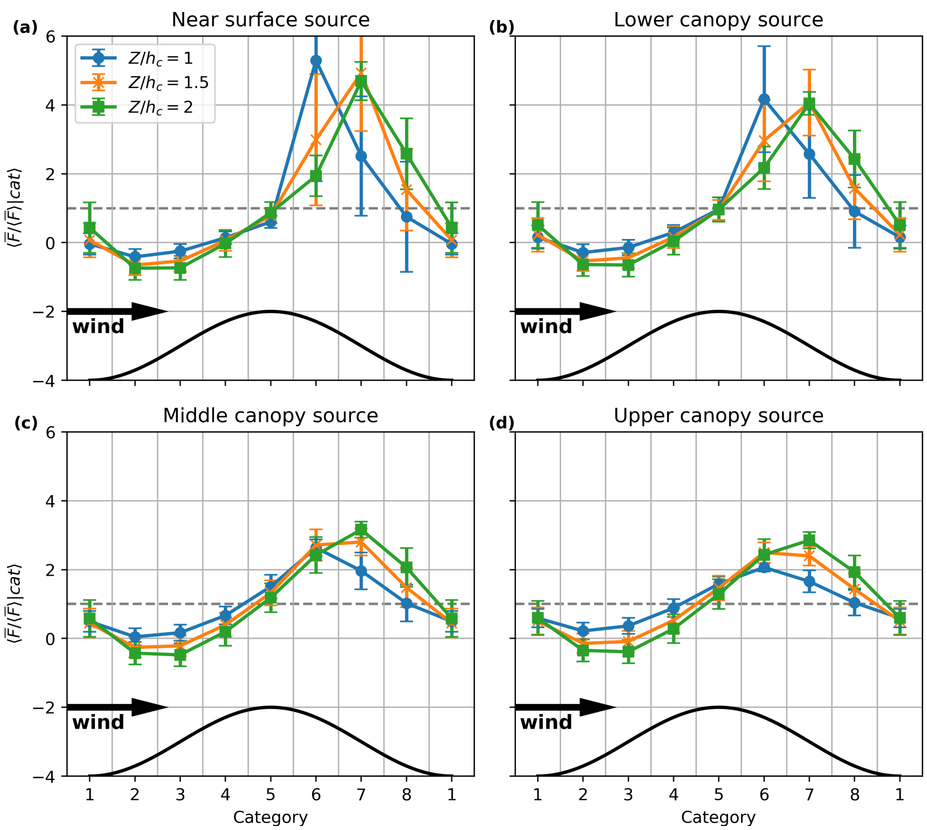

Figure 6. Normalized flux conditionally averaged based on the topography categories for the ideal topography case for different combinations of source layers and sampling heights. Errorbars represent one standard deviation and the gray dashed line indicates the landscape flux.

The true test of the categorization was its application to the real topography (Figure 7). When compared to the ideal topography, the amplitude of the variation in the conditional average flux was smaller and the variability within each category was much larger. This was mostly because in this case there was a very large reduction in complexity introduced by the categorization. All the hills, independently of length, height, and slope received the same treatment. The crosswise topographical information was not taken into account. Despite this simplification, a strong signal was still observed, with significant correlation between negative fluxes in the windward side and flux enhancement in the leeward side of the hills. Increasing the number of categories or including information about the crosswise topography did not seem to improve this relation (not shown).

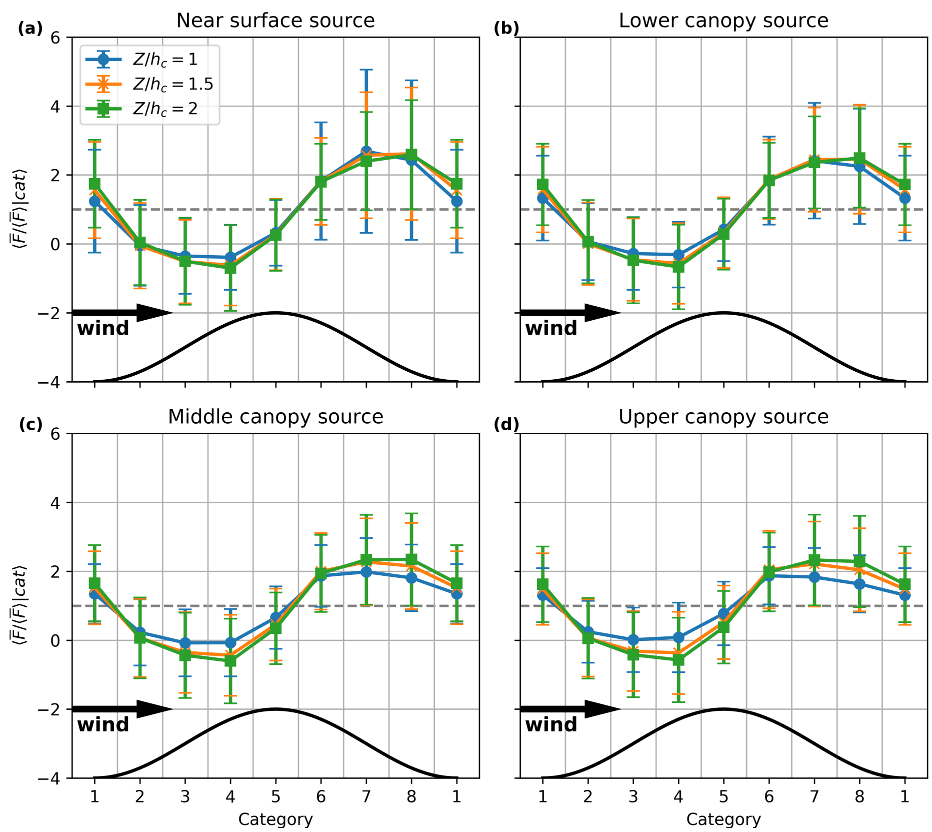

Figure 7. Normalized flux conditionally averaged based on the topography categories for the real topography case for different combinations of source layers and sampling heights. Errorbars represent one standard deviation and the gray dashed line indicates the landscape flux.

To further test the topography categorization, we used the conditional averaged fluxes and the topography categories to “reconstruct” the spatial structure of the fluxes. As an example, we adopted the source from the upper-canopy with sampling at $Z_m/h_c = 2$ as a test case, and simply assigned the mean values in Figure 7d to the topography categories, which resulted in the fluxes shown in Figure 8a. Even though the magnitude of the fluxes were attenuated, this simple procedure was capable of separating regions of flux enhancement and regions of negative flux when compared to the flux obtained directly from the LES (Figure 4d). This was confirmed by the fairly large correlation coefficient between the reconstructed fluxes and the original fluxes (Figure 8c), which indicated that one could predict regions of flux enhancement and regions of negative fluxes only based on the topography category. However, the accompanying large root-mean-square-error (RMSE), which were close to or larger than the mean (Figure 8d), showed that quantitative predictions solely based on the topography may not be possible. For the real topography used here, in which no preferential directions exist, we assumed that the conditional average fluxes were independent of wind direction, and applied the values in Figure 7d with a topography categorized for a different wind direction. As an example, we used a mean wind blowing in the positive y direction, which resulted in the fluxes shown in Figure 8b. This result highlighted the strong impact of wind direction on the spatial patterns of the local flux.

3.4 Generalized footprint analysis

When considering EC measurements over flat heterogeneous landscapes, the footprint analysis plays an important role in placing flux towers so that the measured fluxes are representative of the biome being studied (Finnigan, 2004). Following Schmid (2002), the flux footprint function $\phi_F(\mathbf{x};\mathbf{x}')$ for measurement location $\mathbf{x}$ and source/sink location $\mathbf{x}' = (x', y', Z')$ is defined by

$$F(\mathbf{x}) = \int_{\chi} Q(\mathbf{x}')\phi_F(\mathbf{x};\mathbf{x}')\ \mathrm{d}\mathbf{x}', \tag{2}$$

where $Q(\mathbf{x}')$ is the distribution of source/sink in the vegetation volume χ. In the present case, the vertical extent of the four canopy layers defined in section 2.2 were used for the vertical integration, resulting in footprint functions $\phi_F(x, y, Z_m; Z')$ – two dimensional fields for each pair of canopy source layer (Z') and measurement height (Z_m). To characterize the horizontal extension of the source area, we adopted the source area of level P for measurement location $\mathbf{x}$, denoted by $\Omega_P(x, y, Z_m; Z')$ and defined as the integral of the footprint function over the smallest possible area comprising $P\%$ of the total source influence on the measured signal (Schmid & Oke, 1990; Schmid, 1994). In practice, the footprint function is sorted in decreasing order before integration so that the area to contribute $P\%$ of the total integration is the smallest one. We used $P = 50\%$ to characterize source areas for fluxes corresponding to each pair of source layer and observation height for all 3 simulations (flat, idealized, and real topographies). Spatial patterns of the resulting source areas corresponding to the fluxes shown in Figs. 3 and 4 are presented in the supporting information. In general, regions of negative fluxes tended to have large source areas, and in many cases the chimney regions also had large source areas. However, segregating results based on the 8 topography categories introduced in section 3.3 did not add much predictive value. We only reported the mean source areas $\langle\Omega_{50}\rangle$ in Table 2 (these were calculated from averages over the entire horizontal plane).

For the flat topography simulation, in most cases the source area increased with vertical distance between source height and sampling height. Thus, at a fixed sampling height, the source area increased as the source height was moved lower into the canopy. The presence of topography increased significantly the source area for all pairs of source and sampling heights, and this increase was more accentuated in the real topography than in the idealized case. The latter was associated with the scalar transport by secondary flow circulations in the crosswise direction.

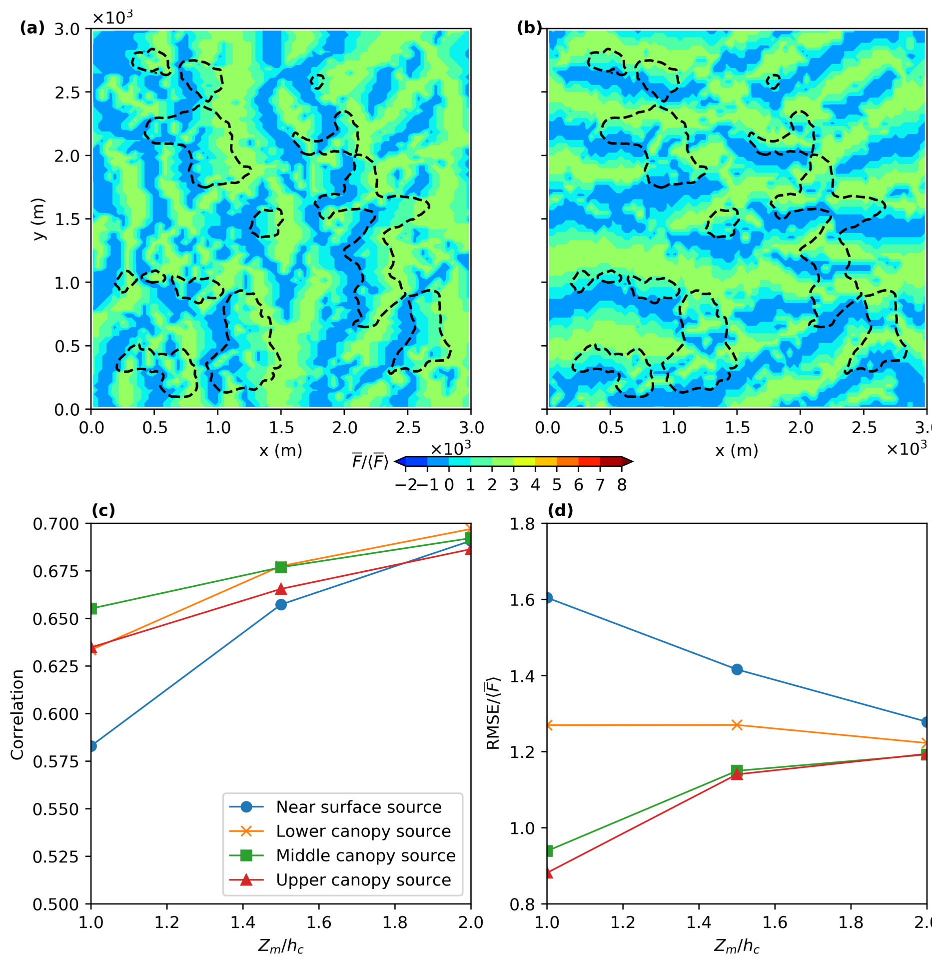

Figure 8. Normalized fluxes estimated from the topography categories for a source in the upper canopy and sampling at $Z_m/h_c = 2.0$ for (a) mean wind from left to right and (b) mean wind from bottom to top. (c) Correlation coefficient and (d) root-mean-square-error (RMSE) between estimated flux shown in (a) and the real flux.

The experience in scalar flux measurements over flat heterogeneous landscapes is that increasing the source area blends signatures of surface heterogeneity thereby increasing the representativeness of the observation (Schmid, 1994). The connection between source area and flux non-uniformity induced by topography was explored by calculating average fluxes and variances as a function of source area (i.e. conditional averages $\langle \overline{F}/\langle \overline{F} \rangle | \Omega_{50} \rangle$ and conditional variances $\langle \left(\overline{F}/\langle \overline{F} \rangle - \langle \overline{F}/\langle \overline{F} \rangle | \Omega_{50} \rangle \right)^2 | \Omega_{50} \rangle$, where the operator $\langle \cdot | \Omega_{50} \rangle$ represents the conditional average based on the value of Ω_{50}; Figure 9). The main feature of the conditional averages was the very large variability (quantified by the large errorbars corresponding to one standard deviation), which pointed to a very low correlation between the magnitude of the flux and the area of the footprint. This result confirmed the difficulty associated with interpreting footprints over complex terrain (Finnigan, 2004), and clearly showed that a larger footprint did not imply a better estimate of the landscape flux. Perhaps a surprising feature in Figure 9 was the fact that the largest fluxes were not necessarily associated with the largest source areas, but that the conditionally averaged flux was very close to the landscape flux when the source area matched the area over flat topography (indicated by the diamonds with black edges in the Figure). Note that in most cases the curves were not monotonic, and very large source areas tended to be associated with regions of negative fluxes.

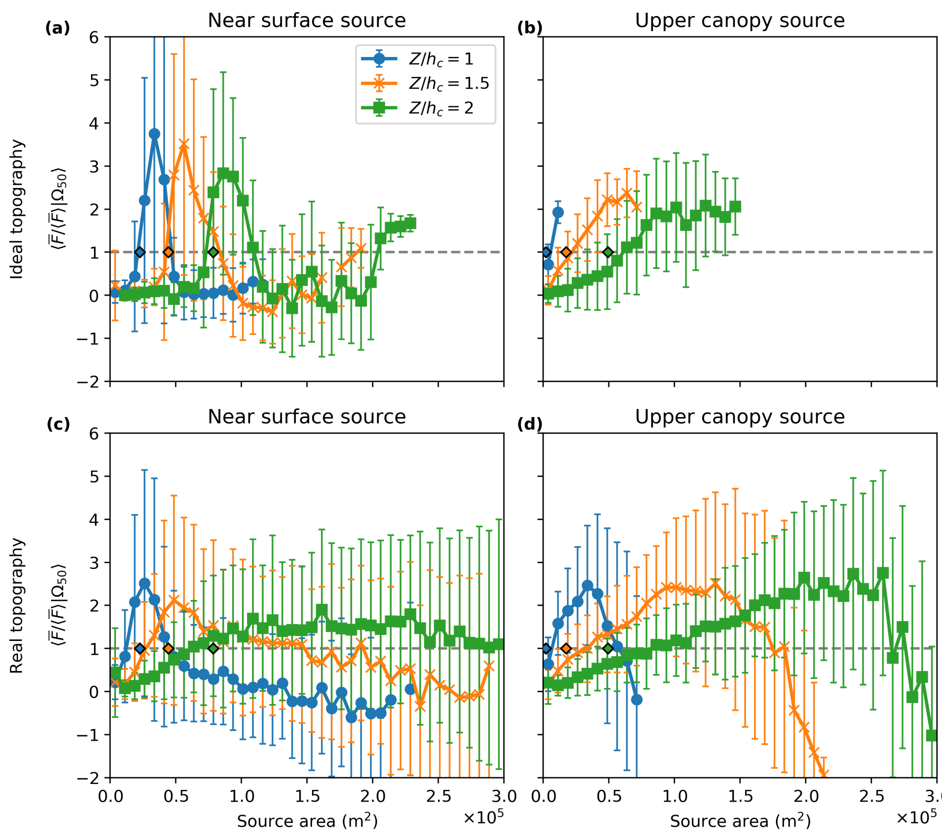

Figure 9. Normalized flux conditionally averaged based on the source area Ω_{50} for ideal and real topography.

4 Conclusions and implications for tower measurements

In this work, LES was used to investigate the influences of gentle topography on the spatial distribution of fluxes of gases emitted uniformly within tall and dense forests.

Before any general conclusions can be drawn, we must emphasize that results presented here were all based on one idealized topography and one realistic topography (note that the idealized topography may be more representative of some real situations with quasi-parallel ridges than the real topography). In addition, all simulations were performed for neutral atmospheric stability. Fluxes were determined in the direction perpendicular to the topography (and to the canopy top), and interpreted as representative of tower-like EC measurements using a planar-fit coordinate system. Simulations were performed for a very dense forest ($LAI = 7$), but we expect results to be applicable as long as the deep canopy criterion $h_c/L_c > 1$ is satisfied. Despite these restrictions, a number of conclusions can be drawn to guide EC observations over forests covering gentle topography. Future studies should focus on effects of atmospheric stability and regional wind patterns induce by topography and surface heterogeneities. Both extensions requires larger simulation domains than the one employed here.

It is clear from the results presented above that, for these conditions, estimating landscape fluxes from a single tower measurement may lead to unacceptably large bias in errors, and that the magnitude of these errors depend on the source height inside the canopy. This is in agreement with the findings from Ross and Harman (2015) for an isolated ridge. Local fluxes can be almost an order of magnitude larger than the landscape flux. In a reasonably large area, they can even have the opposite sign (and a magnitude comparable to the landscape flux). The presence of large negative fluxes may lead one to conclude that the forest is a sink for a particular gas, when it is actually a source. This problem cannot be avoided by increasing sampling height, at least within the range tested here (i.e., up to two canopy heights). In reality, for sources in the middle and upper canopy, the flux heterogeneity actually increases with increasing sampling height.

The other problem is the effect of source height on scalar flux non-uniformity across the hill. The disproportionally strong chimney effect for near surface sources in the lee of hills and ridges can lead to a local dominance of CO2 fluxes from soil respiration and produce positive net fluxes of CO2 in this region despite the overall dominance of photosynthesis at the landscape scale. However, the same effect may have important consequences for interpreting fluxes of other gases with sources that are vertically distributed within the canopy, and it may lead to additional difficulties in partitioning evaporation and evapotranspiration. In principle, one could use numerical simulations to aid in the interpretation of eddy covariance fluxes obtained from tower measurements. In particular, one could develop upscaling factors $UF = \overline{F}/\langle\overline{F}\rangle$ that would yield more robust estimates of landscape fluxes from tower observations (i.e., $\overline{F}_{\mathrm{landscape}} = UF \times \overline{F}_{\mathrm{tower}}$). However, these factors would be specific for each tower and, in principle, a function of atmospheric conditions (such as wind speed and direction and atmospheric stability). The issue with this approach is the requirement of a large number of dedicated high-resolution LES runs. As shown above, it may be possible to devise a simpler method, based the topography categorization. However, at this stage, this is only a blue-print on how to proceed in organizing simulation results rather than offering any finality to the problem at hand.

The general rule-of-thumb of siting towers at the top of hills is not a bad idea from the perspective of topography effects on fluxes. For the idealized topography, the flux at the crest of the ridge is the closest to the landscape flux, and the variability is small (Figure 6). However, the bias can still be large depending on the source and sampling heights (varying between 40% lower to 50% higher than the landscape mean). In the real topography, the situation is more difficult. The crest is still the best location, but now it consistently provides an underestimation of the landscape flux (varying from 22% to 75% of the landscape flux). The variation of fluxes observed at different crests is extremely large, complicating the interpretation of measurements. At the moment, it is unclear if the increased mixing promoted by buoyancy during daytime would alleviate this problem. The presence of topography, even gentle topography, can significantly enlarge the source area and the "apparent" representativeness of the tower-based EC observations. However, this larger footprint does not seem to ameliorate the flux spatial non-uniformity induced by flow structure.

Acknowledgments

This work was supported by the National Science Foundation (NSF-AGS-1644375 to UCLA and NSF-AGS-1644382 to Duke University). The data needed for reproducing the figures are available at the website `https://zenodo.org/record/3774817#.XrsXUGhKhPY` with assigned doi:10.5281/zenodo.3774817. For more questions regarding the dataset and model, please contact chamecki@ucla.edu.

References

Bailey, B. N. (2016). Numerical considerations for lagrangian stochastic dispersion models: Eliminating rogue trajectories, and the importance of numerical accuracy. *Boundary-Layer Meteorology*, *162*(1), 43–70.

Baldocchi, D. (2008). Breathing of the terrestrial biosphere: Lessons learned from a global network of carbon dioxide flux measurement systems. *Australian Journal of Botany*, *56*(1), 1.

Baldocchi, D., Falge, E., Gu, L., Olson, R., Hollinger, D., Running, S., ... Wofsy, S. (2001). FLUXNET: A new tool to study the temporal and spatial variability of ecosystem–scale carbon dioxide, water vapor, and energy flux densities. *Bulletin of the American Meteorological Society*, *82*(11), 2415–2434.

Baldocchi, D., Finnigan, J., Wilson, K., U, K. T. P., & Falge, E. (2000). On measuring net ecosystem carbon exchange over tall vegetation on complex terrain. *Boundary-Layer Meteorology*, *96*(1-2), 257–291.

Belcher, S. E., Harman, I. N., & Finnigan, J. J. (2012). The wind in the willows: Flows in forest canopies in complex terrain. *Annual Review of Fluid Mechanics*, *44*(1), 479–504.

Belcher, S. E., Jerram, N., & Hunt, J. C. R. (2003). Adjustment of a turbulent boundary layer to a canopy of roughness elements. *Journal of Fluid Mechanics*, *488*, 369–398.

Chen, B., Chamecki, M., & Katul, G. G. (2019). Effects of topography on in-canopy transport of gases emitted within dense forests. *Quarterly Journal of the Royal Meteorological Society*, *145*(722), 2101–2114.

Chester, S., Meneveau, C., & Parlange, M. B. (2007). Modeling turbulent flow over fractal trees with renormalized numerical simulation. *Journal of Computational Physics*, *225*(1), 427–448.

Dupont, S., Brunet, Y., & Finnigan, J. (2008). Large-eddy simulation of turbulent flow over a forested hill: Validation and coherent structure identification. *Quarterly Journal of the Royal Meteorological Society*, *134*(636), 1911–1929.

Farr, T. G., Rosen, P. A., Caro, E., Crippen, R., Duren, R., Hensley, S., ... Alsdorf, D. (2007). The shuttle radar topography mission. *Reviews of Geophysics*, *45*(2).

Finnigan, J. J. (2004). The footprint concept in complex terrain. *Agricultural and Forest Meteorology*, *127*(3-4), 117–129.

Finnigan, J. J., & Belcher, S. E. (2004). Flow over a hill covered with a plant canopy. *Quarterly Journal of the Royal Meteorological Society*, *130*(596), 1–29.

Fuentes, J. D., Chamecki, M., dos Santos, R. M. N., Randow, C. V., Stoy, P. C., Katul, G., ... Yañez-Serrano, A. M. (2016). Linking meteorology, turbulence, and air chemistry in the amazon rain forest. *Bulletin of the American Meteorological Society*, *97*(12), 2329–2342.

Gerken, T., Chamecki, M., & Fuentes, J. D. (2017). Air-parcel residence times

within forest canopies. *Boundary-Layer Meteorology*, *165*(1), 29–54.
Grant, E. R., Ross, A. N., & Gardiner, B. A. (2016). Modelling canopy flows over complex terrain. *Boundary-Layer Meteorology*, *161*(3), 417–437.
Grant, E. R., Ross, A. N., Gardiner, B. A., & Mobbs, S. D. (2015). Field observations of canopy flows over complex terrain. *Boundary-Layer Meteorology*, *156*(2), 231–251.
Katul, G., Finnigan, J., Poggi, D., Leuning, R., & Belcher, S. (2006). The influence of hilly terrain on canopy-atmosphere carbon dioxide exchange. *Boundary-Layer Meteorology*, *118*(1), 189–216.
Li, Q., Bou-Zeid, E., & Anderson, W. (2016). The impact and treatment of the gibbs phenomenon in immersed boundary method simulations of momentum and scalar transport. *Journal of Computational Physics*, *310*, 237–251.
Liu, Z., Hu, Y., Fan, Y., Wang, W., & Zhou, Q. (2019). Turbulent flow fields over a 3d hill covered by vegetation canopy through large eddy simulations. *Energies*, *12*(19), 3624.
Liu, Z., Ishihara, T., He, X., & Niu, H. (2016). LES study on the turbulent flow fields over complex terrain covered by vegetation canopy. *Journal of Wind Engineering and Industrial Aerodynamics*, *155*, 60–73.
Lorenz, M. (1905). Methods of measuring the concentration of wealth. *Publications of the American Statistical Association*, *9*, 209–219.
Marques Filho, A. d. O., Dallarosa, R. G., & Pachêco, V. B. (2005). Radiação solar e distribuição vertical de área foliar em floresta-reserva biológica do cuieiras zf2, manaus. *Acta Amazonica*, *35*(4), 427–436.
Pan, Y., Chamecki, M., & Isard, S. A. (2014). Large-eddy simulation of turbulence and particle dispersion inside the canopy roughness sublayer. *Journal of Fluid Mechanics*, *753*, 499–534.
Patton, E. G., & Katul, G. G. (2009). Turbulent pressure and velocity perturbations induced by gentle hills covered with sparse and dense canopies. *Boundary-Layer Meteorology*, *133*(2), 189–217.
Peskin, C. S. (1972). Flow patterns around heart valves: A numerical method. *Journal of Computational Physics*, *10*(2), 252–271.
Poggi, D., & Katul, G. G. (2007). Turbulent flows on forested hilly terrain: The recirculation region. *Quarterly Journal of the Royal Meteorological Society*, *133*(625), 1027–1039.
Poggi, D., Katul, G. G., Finnigan, J. J., & Belcher, S. E. (2008). Analytical models for the mean flow inside dense canopies on gentle hilly terrain. *Quarterly Journal of the Royal Meteorological Society*, *134*(634), 1095–1112.
Ross, A. N. (2011). Scalar transport over forested hills. *Boundary-Layer Meteorology*, *141*(2), 179–199.
Ross, A. N., & Harman, I. N. (2015). The impact of source distribution on scalar transport over forested hills. *Boundary-Layer Meteorology*, *156*(2), 211–230.
Ross, A. N., & Vosper, S. B. (2005). Neutral turbulent flow over forested hills. *Quarterly Journal of the Royal Meteorological Society*, *131*(609), 1841–1862.
Ruck, B., & Adams, E. (1991). Fluid mechanical aspects of the pollutant transport to coniferous trees. *Boundary-Layer Meteorology*, *56*(1-2), 163–195.
Schmid, H. P. (1994). Source areas for scalars and scalar fluxes. *Boundary-Layer Meteorology*, *67*(3), 293–318.
Schmid, H. P. (2002). Footprint modeling for vegetation atmosphere exchange studies: A review and perspective. *Agricultural and Forest Meteorology*, *113*(1-4), 159–183.
Schmid, H. P., & Oke, T. R. (1990). A model to estimate the source area contributing to turbulent exchange in the surface layer over patchy terrain. *Quarterly Journal of the Royal Meteorological Society*, *116*(494), 965–988.
Shaw, R. H., & Schumann, U. (1992). Large-eddy simulation of turbulent flow above and within a forest. *Boundary-Layer Meteorology*, *61*(1-2), 47–64.

Tóta, J., Fitzjarrald, D. R., & da Silva Dias, M. A. F. (2012). Amazon rainforest exchange of carbon and subcanopy air flow: Manaus LBA site—a complex terrain condition. *The Scientific World Journal*, *2012*, 1–19.

Weil, J. C., Sullivan, P. P., & Moeng, C.-H. (2004). The use of large-eddy simulations in lagrangian particle dispersion models. *Journal of the Atmospheric Sciences*, *61*(23), 2877–2887.

Werner, M. (2001). Shuttle radar topography mission (SRTM) mission overview. *Frequenz*, *55*(3-4).

Wood, N. (1995). The onset of separation in neutral, turbulent flow over hills. *Boundary-Layer Meteorology*, *76*(1-2), 137–164.